Flow of Mantle Fluids Through the Ductile Lower Crust: Helium Isotope Trends

B. Mack Kennedy, *et al.*

Science **318**, 1433 (2007);
DOI: 10.1126/science.1147537

can be expected that $\mathbf{E} \perp \mathbf{B}_{ext}$. In that experiment, no coherent oscillations were observed, which is consistent with the considerations here.

An important characteristic of spin orbit–mediated driving is the linear dependence of the effective driving field on the external magnetic field, which follows from Eq. 1 and is predicted in (*12*, *13*, *29*). We aim to verify this dependence by measuring the Rabi frequency as a function of the resonant excitation frequency (Fig. 4A), which is proportional to the external magnetic field. Each point is rescaled by the estimated applied electric field (Fig. 4B). Even at fixed output power of the microwave source, the electric field at the dot depends on the microwave frequency due to various resonances in the line between the microwave source and the gate (caused by reflections at the bonding wires and microwave components). However, we use the photon-assisted–tunneling response as a probe for the ac voltage drop across the interdot tunnel barrier, which we convert into an electric field amplitude by assuming a typical interdot distance of 100 nm. This allows us to roughly estimate the electric field at the dot for each frequency (*17*). Despite the large error bars, which predominantly result from the error made in estimating the electric field, an overall upward trend is visible in Fig. 4A.

For a quantitative comparison with theory, we extract the spin-orbit strength in GaAs, via the expression of the effective field $\mathbf{B}_{eff}$ perpendicular to $\mathbf{B}_{ext}$ for the geometry of this experiment (*12*)

$$|\mathbf{B}_{eff}(t)| = 2\,|\mathbf{B}_{ext}|\,\frac{l_{dot}}{l_{SO}}\,\frac{e|\mathbf{E}(t)|l_{dot}}{\Delta} \qquad (2)$$

with l_{SO} the spin-orbit length (for the other definitions, see Fig. 1B). Here, $l_{SO}^{-1} = m^*(\alpha \mp \beta)/\hbar$ for the case with the gate symmetry axis along $[1\bar{1}0]$ or [110], respectively. Via $f_{Rabi} = (g\mu_B|\mathbf{B}_{eff}|)/2h$, the confidence interval of the slope in Fig. 4A gives a spin-orbit length of 28 to 37 μm (with a level splitting Δ in the right dot of 0.9 meV extracted from high-bias transport measurements). Additional uncertainty in l_{SO} is due to the estimate of the interdot distance and the assumption of a homogeneous electric field, deformation effects of the dot potential (*15*), and extra cubic terms in the Hamiltonian (*7*). Still, the extracted spin-orbit length is of the same order of magnitude as other reported values for GaAs quantum dots (*18*).

Both the observed trend of $\mathbf{B}_{eff}$ with f_{ac} and the extracted range for l_{SO} are consistent with our supposition (by elimination of other mechanisms) that spin transitions are mediated by spin-orbit interaction. We note that also for relaxation of single electron spins in which electric field fluctuations from phonons couple to the spin, it is by now well established that the spin-orbit interaction is dominant at fields higher than a few 100 mT (*12*, *18*, *28*, *29*). It can thus be expected to be dominant for coherent driving as well.

The electrically driven single-spin resonance reported here, combined with the so-called $\sqrt{SWAP}$ gate based on the exchange interaction between two neighboring spins (*30*), brings all-electrical universal control of electron spins within reach. Whereas the $\sqrt{SWAP}$ gate already operates on subnanosecond time scales, single-spin rotations still take about 100 ns (the main limitation is photon-assisted tunneling). Faster operations could be achieved by suppressing photon-assisted tunneling (e.g., by increasing the tunnel barriers or operating deeper into Coulomb blockade), by working at still higher magnetic fields, by using materials with stronger spin-orbit interaction, or through optimized gate designs. Furthermore, the electrical control offers the potential for spatially selective addressing of individual spins in a quantum dot array, because the electric field is produced by a local gate. Finally, the spin rotations were realized at magnetic fields high enough to allow for single-shot read-out of a single spin (*31*), so that both elements can be integrated in a single experiment.

References and Notes

1. D. Awschalom, D. Loss, N. Samarth, *Semiconductor Spintronics and Quantum Computation* (Springer-Verlag, Berlin, 2002).
2. C. Poole, *Electron Spin Resonance* (Wiley, New York, ed. 2, 1983).
3. B. Simovič *et al.*, *Rev. Sci. Instrum.* **77**, 064702 (2006).
4. F. H. L. Koppens *et al.*, *Nature* **442**, 766 (2006).
5. Y. Tokura, W. G. Van der Wiel, T. Obata, S. Tarucha, *Phys. Rev. Lett.* **96**, 047202 (2006).
6. Y. A. Bychkov, E. I. Rashba, *J. Phys. C* **17**, 6039 (1984).
7. G. Dresselhaus, *Phys. Rev.* **100**, 580 (1955).
8. Y. Kato, R. C. Myers, A. C. Gossard, D. D. Awschalom, *Nature* **427**, 50 (2003).
9. Y. Kato *et al.*, *Science* **299**, 1201 (2003).
10. G. Salis *et al.*, *Nature* **414**, 619 (2001).
11. M. Schulte, J. G. S. Lok, G. Denninger, W. Dietsche, *Phys. Rev. Lett.* **94**, 137601 (2005).
12. V. N. Golovach, M. Borhani, D. Loss, *Phys. Rev. B* **74**, 165319 (2006).
13. L. Levitov, E. Rashba, *Phys. Rev. B* **67**, 115324 (2003).
14. S. Debald, C. Emary, *Phys. Rev. Lett.* **94**, 226803 (2005).
15. J. Walls, *Condens. Matter*, http://arxiv.org/abs/0705.4231 (2007).
16. F. H. L. Koppens *et al.*, *J. Appl. Phys.* **101**, 081706 (2007).
17. Supporting material is available on *Science* Online.
18. R. Hanson, L. P. Kouwenhoven, J. R. Petta, S. Tarucha, L. M. K. Vandersypen, *Rev. Mod. Phys.* **79**, 1217 (2007).
19. A. V. Khaetskii, D. Loss, L. Glazman, *Phys. Rev. Lett.* **88**, 186802 (2002).
20. I. A. Merkulov, A. L. Efros, M. Rosen, *Phys. Rev. B* **65**, 205309 (2002).
21. A. C. Johnson *et al.*, *Nature* **435**, 925 (2005).
22. F. H. L. Koppens *et al.*, *Science* **309**, 1346 (2005).
23. J. Baugh, Y. Kitamura, K. Ono, S. Tarucha, *Phys. Rev. Lett.* **99**, 096804 (2007).
24. M. S. Rudner, L. S. Levitov, *Phys. Rev. Lett.* **99**, 036602 (2007).
25. D. Klauser, W. A. Coish, D. Loss, *Phys. Rev. B* **73**, 205302 (2006).
26. E. A. Laird *et al.*, *Condens. Matter*, http://arxiv.org/abs/0707.0557 (2007).
27. F. H. L. Koppens *et al.*, *Phys. Rev. Lett.* **99**, 106803 (2007).
28. S. I. Erlingsson, Y. V. Nazarov, *Phys. Rev. B* **66**, 155327 (2002).
29. A. V. Khaetskii, Y. V. Nazarov, *Phys. Rev. B* **64**, 125316 (2001).
30. J. R. Petta *et al.*, *Science* **309**, 2180 (2005).
31. J. M. Elzerman *et al.*, *Nature* **430**, 431 (2004).

32. We thank L. P. Kouwenhoven, C. Barthel, E. Laird, M. Flatté, I. T. Vink, and T. Meunier for discussions and R. Schouten, B. van der Enden, and R. Roeleveld for technical assistance and J. H. Plantenberg and P. C. de Groot for help with microwave components. Supported by the Dutch Organization for Fundamental Research on Matter (FOM) and the Netherlands Organization for Scientific Research (NWO).

Supporting Online Material

www.sciencemag.org/cgi/content/full/1148092/DC1
Materials and Methods
SOM Text
Figs. S1 and S2
References

20 July 2007; accepted 16 October 2007
Published online 1 November 2007;
10.1126/science.1148092
Include this information when citing this paper.

Flow of Mantle Fluids Through the Ductile Lower Crust: Helium Isotope Trends

B. Mack Kennedy[1] and Matthijs C. van Soest[2]

Heat and mass are injected into the shallow crust when mantle fluids are able to flow through the ductile lower crust. Minimum $^3He/^4He$ ratios in surface fluids from the northern Basin and Range Province, western North America, increase systematically from low crustal values in the east to high mantle values in the west, a regional trend that correlates with the rates of active crustal deformation. The highest ratios occur where the extension and shear strain rates are greatest. The correspondence of helium isotope ratios and active transtensional deformation indicates a deformation-enhanced permeability and that mantle fluids can penetrate the ductile lithosphere, even in regions where there is no substantial magmatism. Superimposed on the regional trend are local, high $^3He/^4He$ anomalies indicating hidden magmatic activity and/or deep fluid production with locally enhanced permeability, identifying zones with high resource potential, particularly for geothermal energy development.

Mantle volatiles, principally water and CO_2, play an important role in lithospheric rheology and the production of buoyant fluids that can be injected into the shallow crust. Regional and local trends in the crustal occurrence of mantle volatiles provide insight into the coupling between mantle-crust tectonics (*1*, *2*), heat and mass exchange between the mantle and crust (*3*–*5*), and the occurrence and distribution of economic resources

such as ore minerals and oil, gas, and geothermal fluids (*6*). Mantle-derived volatiles in the crust are traceable through He isotopic compositions of hydrologic fluids (*7*). Once injected into a crustal-fluid system, mantle He will be continuously diluted with radiogenic helium-4 (^{4}He) acquired from the U,Th–rich crust, and therefore surface-fluid He isotopic compositions also provide a measure of the mantle He flux and the integrated permeability-fluid pressure gradient (flow rate) through the crust (*1*). To enter the hydrologic system, mantle He must pass through a ductile lower crust, which is believed to be an impermeable boundary because of an inability to maintain open fractures on long time scales (*8*–*10*). A general assumption is that the passage of fluids through this boundary must occur either by direct intrusion and degassing of mantle-derived magmas (*6*) or by diffusion through the ductile boundary layer (*11*). However, two recent studies in areas void of recent volcanism (*1*, *12*) have found evidence for fault-controlled advective flow of mantle fluids through the ductile boundary. How and why this occurs is not well understood.

We conducted a regional study of He isotopic compositions of thermal fluids collected from surface features and wells throughout the northern Basin and Range Province (B&R), western North America (Fig. 1 and table S1) (*13*). As a result of the tectonic influence exerted by the relative motion of the Pacific and North American Plates (*14*, *15*), the B&R is a vast extended region of anomalous thermal gradients, large heat flux, high regional elevation, thin (ned) crust, and lithospheric- and asthenospheric-mantle melting. Presently, extension is accommodated by high-angle normal faults, and the locus of major extension and its associated magmatism occurs at the margins of the province (*16*), primarily within the Walker Lane, a narrow 100-to-200–km–wide transtensional volcanic zone along the eastern side of the Sierra Nevada that extends north into a transitional zone between the Sierra Nevada and the subduction-related volcanic arc of the Cascades. East of the Walker Lane, B&R extension occurs at a slowing rate, over a much wider area and in the absence of active or recently active volcanism. The highest extension rates in this area occur west of the central Nevada seismic belt (CNSB), a north-northeast–trending belt of Holocene seismic activity.

Across the northern B&R, three general He isotope trends are apparent. First, ratios >3.0 Ra (*7*) occur only at the western margin of the B&R, reflecting active or recently active shallow-crustal volcanism within the Walker Lane (Coso, Long Valley, and Steamboat) and the Cascade volcanic chain (Lassen, Mount Shasta, Medicine Lake, Crater Lake, and Newberry Crater). Second, the preponderance of ratios >0.6 Ra occur in the northwest B&R in an area ranging from the CNSB west to the transition zone with the Cascade volcanics. Third, east of the CNSB, the He ratios decline, ranging from 0.1 to 0.3 Ra.

Collectively, the minimum ^{3}He/^{4}He ratios define a regional baseline trend of decreasing ratios from west to east, as illustrated by the shaded

[1]Center for Isotope Geochemistry, Earth Sciences Division, Lawrence Berkeley National Laboratory, Berkeley, CA 94720, USA. [2]Noble Gas Geochemistry and Geochronology Laboratory, School of Earth and Space Exploration, Arizona State University, Tempe, AZ 85287–1404, USA.

*To whom correspondence should be addressed. E-mail: bmkennedy@lbl.gov

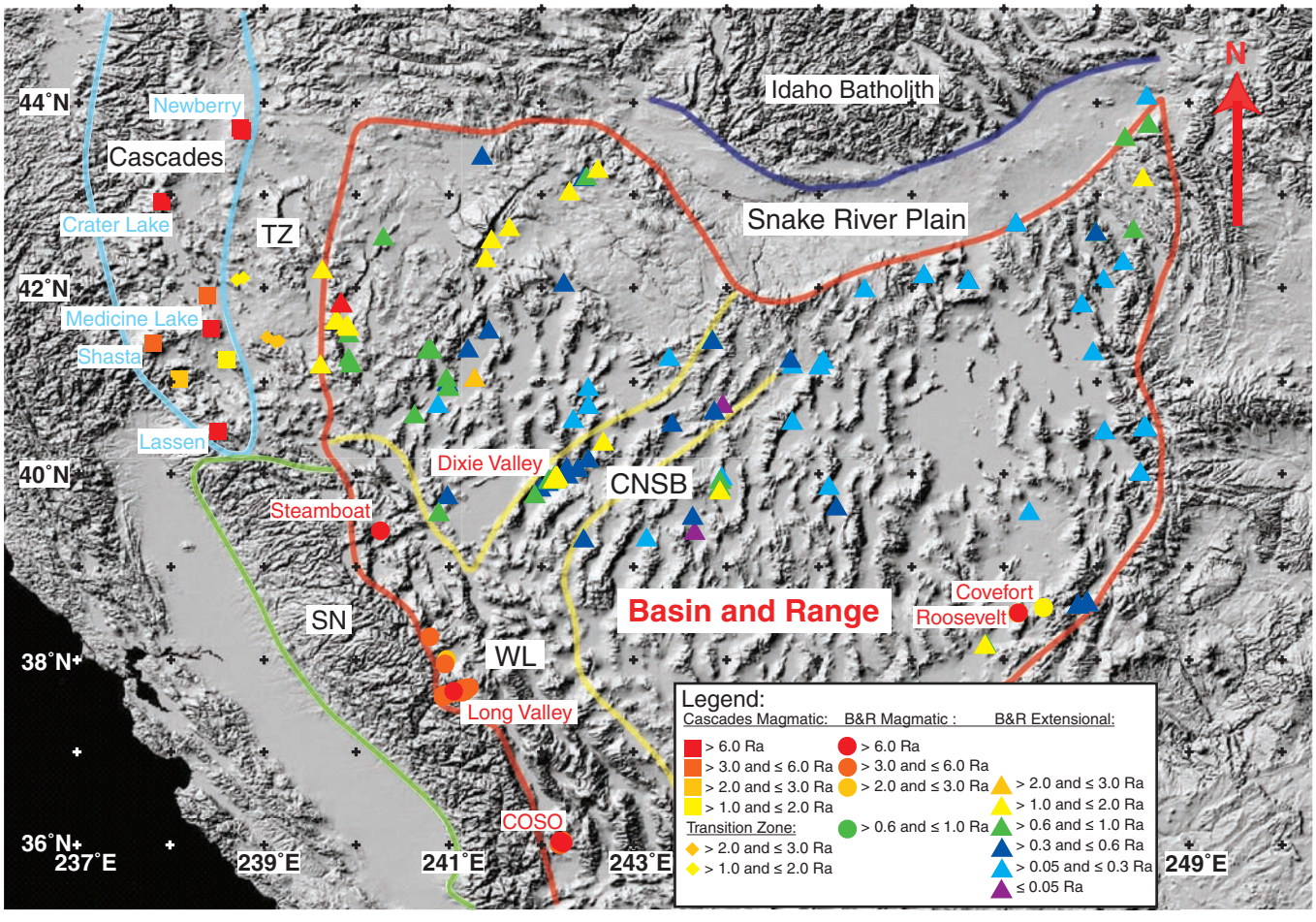

Fig. 1. Sample location map of the B&R and surrounding areas. The symbol colors delineate ^{3}He/^{4}He ratios, expressed as Rc/Ra (the air-corrected sample ratio normalized to the ratio in air), and the symbol shapes identify the type of thermal area. Tectonic zones are outlined: red, northern B&R; yellow, the Walker Lane transtensional zone (WL) and the CNSB; green, the Sierra Nevada batholith (SN); and light blue, the Cascades volcanic zone. TZ, transition zone between the Cascades, WL, and B&R.

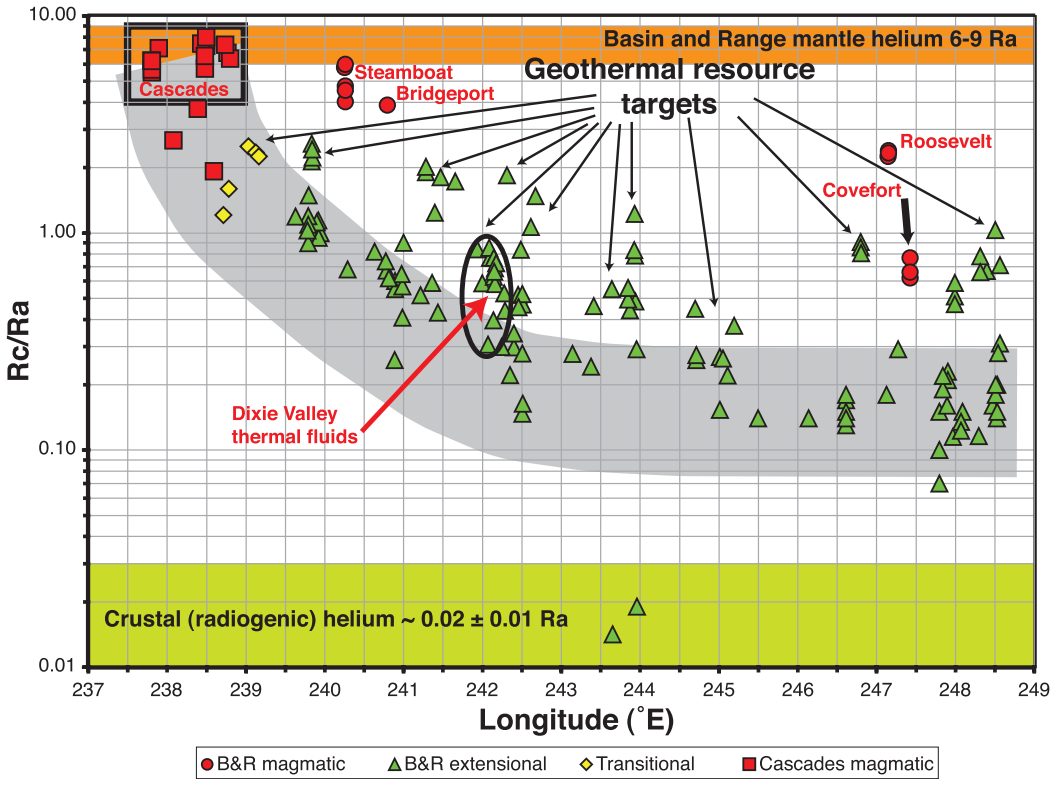

Fig. 2. Air-corrected He isotopic composition of geothermal fluids above 38°N latitude in the B&R, TZ, and Cascades, plotted as a function of longitude. The shaded curve depicts an east-to-west baseline trend defined by minima in the local $^{3}He/^{4}He$ ratios.

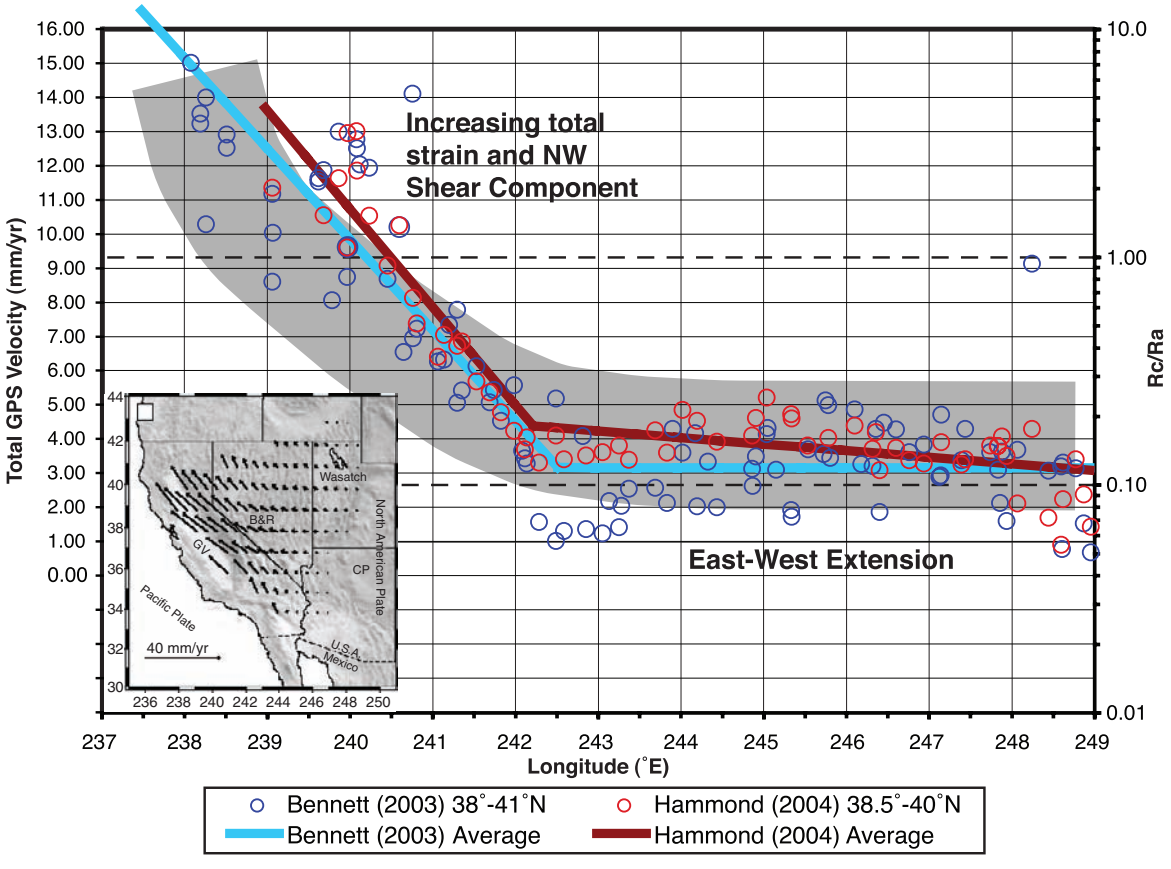

Fig. 3. Compilation of present-day GPS strain rates across the northern B&R, relative to the North America reference frame. The data are from GPS networks located in a band from 38°N to 41° N latitude (*15*, *16*). West of 242°E to 242.5° E longitude, the data show a combined increase in total magnitude of strain and an increase in lateral dextral shear strain superimposed on the east-west extension. This is most evident in the Walker Lane, but it impacts most of the B&R in and to the northwest of the CNSB, as illustrated by the Fig. 3 insert taken from (*19*). The broad colored band is the regional baseline He isotope trend from Fig. 2, shown superimposed on the trends in strain rate. CP, Colorado Plateau; GV, Great Valley.

band in Fig. 2. East of the Walker Lane and Cascades, the occurrence of mantle He—as indicated by baseline $^3He/^4He$ ratios (~0.2 to 2.0 Ra) that are much greater than those of average crustal He (~0.02 Ra)—is not supported by magma intrusion, as this region has no evidence for current or recent volcanic activity. Instead, the baseline trend is strongly correlated with a change in the direction and magnitude of strain detected by present-day Global Positioning System (GPS) velocities (Fig. 3) (*17*, *18*). West of the CNSB, a nearly pure east-west extension rate of ~3 mm/year shifts to N40°W and increases to 12 to 13 mm/year. The accelerating dextral shear component is driven by a drag force due to the relative movement of the Pacific and North American Plates (*19*). We hypothesize that the increase in total strain and, specifically, the northwest-orientated dextral shear component greatly enhance average fluid-flow rates, allowing for a more rapid flow of mantle fluids through the crust and preserving the high $^3He/^4He$ ratios observed at the surface. The enhanced flow rate must persist through the brittle-ductile transition, through the ductile lower crust, and into the mantle lithosphere. If, as expected, fluids passing through the ductile crust enter the base of the brittle zone at, or near, lithostatic pressure, then the east-to-west increase in the flow rate is primarily governed by an east-to-west increase in average permeability.

The high-angle normal faults that presently accommodate B&R extension and that are probably fluid-flow pathways are not expected to penetrate the ductile lower crust. In extensional regimes, because of gravitational loading, the maximum principle stress is perpendicular to the geoid. With increasing depth, the brittle-to-ductile shift in rheology refracts the maximum stress acting on the fault, resulting in nearly horizontal shear zones or detachment faults at the boundary between the high-viscosity upper crusts and low-viscosity lower crusts (*20*, *21*). Strain localization induced by an increasing dextral shear component superimposed on the extensional stress field must mechanically couple the brittle and ductile crustal zones, generating vertically oriented downward fault splays that extend through the ductile crust and into the mantle. These splays would act as conduits for fluid flow. The close correspondence between He isotope ratios and the rate of dextral shear strain suggests that fluid-flow rate (and hence, permeability) through the ductile zone is a function of the rate of dextral shear strain. Once the flow has initiated, the high-pressure pore and fracture fluids may help to maintain permeability, enhancing flow through the ductile zone (*22*).

There are many sampled features that have elevated $^3He/^4He$ ratios with respect to the regional baseline trend. Although a few, such as Roosevelt Hot Spring and Covefort, are associated with crustal magma systems (*23*), the majority are not. An example of the latter is the Dixie Valley thermal system (Fig. 2), where a detailed study (*24*) found a range in He isotope ratios (~0.3 to 0.8 Ra), with the highest ratios restricted to fluids emerging directly from the Stillwater range-front fault system, a high-angle normal fault that defines the western margin of the valley. A recent east-west high-resolution deep magnetotelluric study that crossed through Dixie Valley revealed a zone of low resistance, a possible indication of fluids at a depth of ~25 km within the mantle lithosphere (*25*), suggesting that the Dixie Valley He anomaly reflects a combination of local, deep production of mantle fluids (zone of low resistance) and a range-front fault system with enhanced permeability (high fluid-flow rates and, hence, high $^3He/^4He$ ratios). The range-front fault is the primary conduit supplying $\sim 20 \times 10^9$ kg of 250°C water in support of a 62–megawatt-electric geothermal power plant (*26*). It follows that other "local He anomalies" may be indicative of similar systems and represent geothermal targets with high potential.

Our regional He isotope study of fluids across the northern B&R clearly demonstrates a strong correlation between an east-to-west increase in the magnitude of dextral shear strain and an east-to-west increase in baseline He isotope ratios. In the absence of active or recently active magmatism, the elevated He isotope ratios require amagmatic flow of mantle fluids through the ductile lower crust, suggesting that the increase in dextral shear strain rates creates and maintains permeable pathways through the ductile zone. Elevated He isotope ratios in surface fluids along amagmatic sections of the San Andreas fault (*1*) and a recently observed series of nonvolcanic tremors deep (20 to 40 km) beneath the same section of the fault provide additional support for the existence of deep-mantle fluids, their potential importance in fault mechanisms (*27*), and nonmagmatic fluid flow through the ductile zone.

The high $^3He/^4He$ anomalies superimposed on the regional trend indicate enhanced crustal permeability coupled with local zones of deep fluid production and/or hidden magmatic activity. These local anomalies may be indicative of a heterogeneous distribution of mantle volatiles that promote melt production. Assuming a $CO_2/^3He$ ratio of $\sim 2 \times 10^9$ M (characteristic of mid-ocean ridge basalts) (*6*) as a proxy for mantle-derived volatiles, the calculated fluid-flow rate through the Dixie Valley geothermal system (*24*) translates into a mantle CO_2 flux of $\sim 2 \times 10^{-6}$ to 20×10^{-6} mol cm^{-2} $year^{-1}$. As of yet, no definitive geochemical or isotopic evidence for the presence of mantle CO_2 has been found, other than carbon isotopic compositions ($\delta^{13}C = -6.5 \pm 2.5$ per mil) (*22*) not dissimilar from those of mantle CO_2 (*6*). An estimated $CO_2/^3He$ ratio in Dixie Valley fluids of $\sim 40 \times 10^9$ (*13*) is ~20 times the mid-ocean ridge value, suggesting that most (~95%) of the CO_2 is not mantle-derived or, alternatively, that the subcontinental mantle $CO_2/^3He$ ratio is much greater than that observed at mid-ocean ridges.

Earth's crust stores an enormous resource of thermal energy produced primarily from the radioactive decay of U, Th, and K that is dispersed throughout Earth. It has been estimated that, within the United States (excluding Hawaii and Alaska), there are $\sim 9 \times 10^{16}$ kilowatt-hours (kWh) of accessible geothermal energy. This is a sizable resource compared to the total energy consumption in the United States of 3×10^{13} kWh annually. In order for geothermal systems to develop and mine the heat source naturally, adequate fluid sources and deep permeable pathways are a necessity. The deep pathways provide access to high temperatures that can drive fluid convection cells. He isotopes provide a quantitative or, at least, a qualitative estimate of deep permeability from surface measurements, and anomalies superimposed on regional trends can identify potential resources.

References and Notes

1. B. M. Kennedy *et al.*, *Science* **278**, 1278 (1997).
2. D. L. Newell *et al.*, *GSA Today* **15**, 4 (2005).
3. F. J. Spera, *Contrib. Mineral. Petrol.* **88**, 217 (1984).
4. G. Holland, C. J. Ballentine, *Nature* **441**, 186 (2006).
5. C. J. Ballentine, B. Marty, B. S. Lollar, M. Cassidy, *Nature* **433**, 33 (2005).
6. C. J. Ballentine, R. Burgess, B. Marty, *Rev. Mineral. Geochem.* **47**, 539 (2002).
7. Without mantle influence, crustal fluids are dominated by ^4He produced from the natural radioactivity of U and Th and characterized by very low $^3He/^4He$ ratios of ~0.02 Ra (where Ra = 1.4×10^{-6}, the ratio in air). Mantle fluids without substantial crustal influence are strongly enriched in ^3He, with typical ratios ranging from ~6 to 35 Ra, depending on the mantle source (e.g., plume volcanism versus mid-ocean ridge basalt versus back-arc volcanism).
8. J. D. Byerlee, *Geophys. Res. Lett.* **17**, 2109 (1990).
9. J. D. Byerlee, *Geology* **21**, 303 (1993).
10. N. H. Sleep, M. L. Blanpied, *Nature* **359**, 687 (1992).
11. T. Torgersen, *J. Geophys. Res.* **98**, 16257 (1993).
12. J. T. Kulongoski, D. R. Hilton, J. A. Izbicki, *Geochim. Cosmochim. Acta* **69**, 3857 (2005).
13. Materials and methods are available as supporting material on *Science* Online.
14. C. H. Jones *et al.*, *Tectonphysics* **213**, 57 (1992).
15. M. L. Zoback, G. A. Thompson, *Geology* **6**, 111 (1978).
16. T. Parsons, in *Developments in Geotectonics 25, Publication #264 of the International Lithosphere Program*, K. H. Olsen, Ed. (Elsevier, New York, 1995), pp. 277–324.
17. R. A. Bennett, B. P. Wernicke, N. A. Niemi, A. M. Friedrich, J. L. Davis, *Tectonics* **22**, 1008 (2003).
18. W. C. Hammond, W. Thatcher, *J. Geophys. Res.* **109**, B08403 (2004).
19. L. M. Flesch, W. E. Holt, A. J. Haines, B. Shen-Tu, *Science* **287**, 834 (2000).
20. G. A. Bradshaw, M. D. Zoback, *Geology* **16**, 271 (1988).
21. H. J. Melosh, *Nature* **343**, 331 (1990).
22. S. F. Cox, *Earth Planets Space* **54**, 1121 (2002).
23. D. L. Nielson, J. N. Moore, *Geotherm. Resour. Counc. Trans.* **3**, 503 (1979).
24. B. M. Kennedy, M. C. van Soest, *Geothermics* **35**, 26 (2006).
25. P. E. Wannamaker, W. M. Doerner, D. P. Hasterok, *Geol. Soc. Am. Abstr. Prog.* **37**, 495 (2005).
26. D. D. Blackwell, B. Gollan, D. Benoit, *Geotherm. Resour. Counc. Trans.* **24**, 223 (2000).
27. R. M. Nadeau, D. Dolenc, *Science* **307**, 389 (2005); published online 9 December 2004 (10.1126/science.1107142).

28. This work was supported by the U. S. Department of Energy, Office of Basic Energy Sciences and Office of Geothermal Technologies under contract DE-AC02-05CH11231.

Supporting Online Material

www.sciencemag.org/cgi/content/full/318/5855/1433/DC1
Materials and Methods
Table S1
References

9 July 2007; accepted 17 October 2007
10.1126/science.1147537